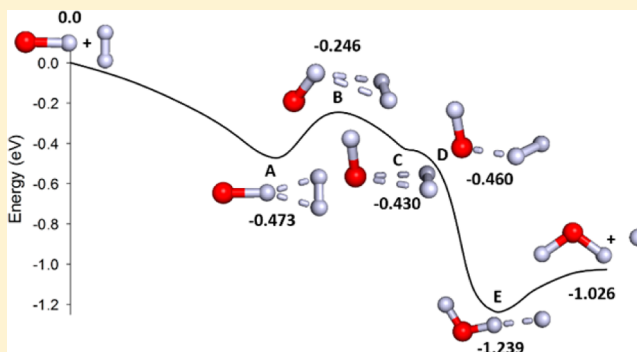


Rotational and Isotopic Effects in the $\text{H}_2 + \text{OH}^+ \rightarrow \text{H} + \text{H}_2\text{O}^+$ ReactionHongwei Song,[†] Anyang Li,[‡] and Hua Guo^{*}

Department of Chemistry and Chemical Biology, University of New Mexico, Albuquerque, New Mexico 87131, United States

ABSTRACT: Initial state selected time-dependent wave packet and quasi-classical trajectory methods are employed to study the effects of reactant rotational excitations and isotopic substitutions on the title reaction. The coupled-channel (CC) and/or centrifugal sudden (CS) integral cross sections are calculated quantum mechanically. It was found that the CS cross sections are slightly smaller than the CC counterparts over the collision energy range studied. The quantum dynamical and quasi-classical trajectory results agree reasonably well and both indicate that the rotational excitation of H_2 enhances the reaction in all energies, whereas the rotational excitation of OH^+ promotes the reaction more strongly at low collision energies but has a negligible effect at high collision energies. In addition, there exist significant isotopic substitution effects: The reaction cross section of the $\text{D}_2 + \text{OH}^+$ reaction is much lower than those of the $\text{H}_2 + \text{OH}^+$ and $\text{HD} + \text{OH}^+$ reactions, which are quite close.



I. INTRODUCTION

Ion–molecule reactions have attracted considerable attention of both theoretical and experimental researchers in the last several decades owing to their important role in many fields, such as interstellar processes,¹ electric discharges,² and planetary ionospheres.³ Recent advances in experimental techniques have enabled detailed measurements of both integral⁴ and differential cross sections⁵ of some prototypical ion–molecule reactions, posing a challenge to accurate theoretical characterization of the reaction dynamics. This experiment–theory interplay has helped to provide a more in-depth understanding of issues pertaining to microscopic reaction mechanism and dynamics.^{6,7}

In this publication, we focus on the reaction between $\text{OH}^+(\tilde{X}^3\Sigma^-)$ and $\text{H}_2(\tilde{X}^1\Sigma_g^+)$, which leads to the formation of $\text{H}^{(2)}\text{S} + \text{H}_2\text{O}^+(\tilde{X}^2\text{B}_1)$. This is an important step in the interstellar formation of the H_xO^+ ($x = 1, 2, 3$) species,^{8–10} which have recently been found in various interstellar media by the powerful Herschel space telescope.^{11–13} In addition to its astrochemical interest, this reaction also serves as a prototype in understanding reaction dynamics of ion–molecule reactions.¹⁴ The $\text{H}_2 + \text{OH}^+ \rightarrow \text{H} + \text{H}_2\text{O}^+$ reaction mainly takes place adiabatically via the lowest triplet PES at low energies, of which the full-dimensional potential energy surface (PES) has recently been developed on the basis of a permutation invariant polynomial-neural network (PIP-NN)^{15,16} fit of $\sim 30\,000$ points calculated at the Davidson-corrected multireference configuration interaction level with the aug-cc-pVQZ basis set.¹⁷ Particular attention has been paid to the long-range interactions between the two reactants to make sure the proper behavior. More recently, the thermal rate coefficients for the title reaction and its isotopologue have been computed on this PES at several

temperatures and they agree with experimental values very well,¹⁴ underscoring the accuracy of the PES.

The reaction pathway on the ab initio based PES for the title reaction, which is shown in Figure 1a, bears much similarity to that of the reaction between H_2O^+ and H_2 .^{18,19} Both reactions are exothermic and characterized by a submerged barrier and a shallow well in the product channel. Ng and co-workers have studied the $\text{H}_2\text{O}^+ + \text{H}_2$ reaction and found surprising enhancements of the reaction by rotational excitations of the H_2O^+ reactant, particularly at low collision energies.^{18,20,21} This rotational effect was also found to result in a unique temperature dependence of the rate coefficient.²² The enhancement was attributed to coupling of the rotational mode of the H_2O^+ reactant with the reaction coordinate at the submerged saddle point,¹⁹ according to our recently proposed sudden vector projection (SVP) model.^{23,24} Interestingly, a SVP analysis for the title reaction also predicts a strong rotational effects for the OH^+ reactant,¹⁷ which has been implicated in our recent combined experiment–theory study of the thermal rate coefficients using a quasi-classical trajectory (QCT) method.¹⁴ In this publication, we report the first initial state specific quantum dynamical (QD) calculations on the title reaction on the same PES, supported by additional QCT calculations. Such full-dimensional QD calculations have never been attempted for any ion–molecule reaction with more than three atoms, because of the huge computational costs needed to cover the long-range interaction between the reactants. This paper is

Special Issue: Piergiorgio Casavecchia and Antonio Lagana Festschrift

Received: November 26, 2015

Revised: January 3, 2016

Published: January 5, 2016

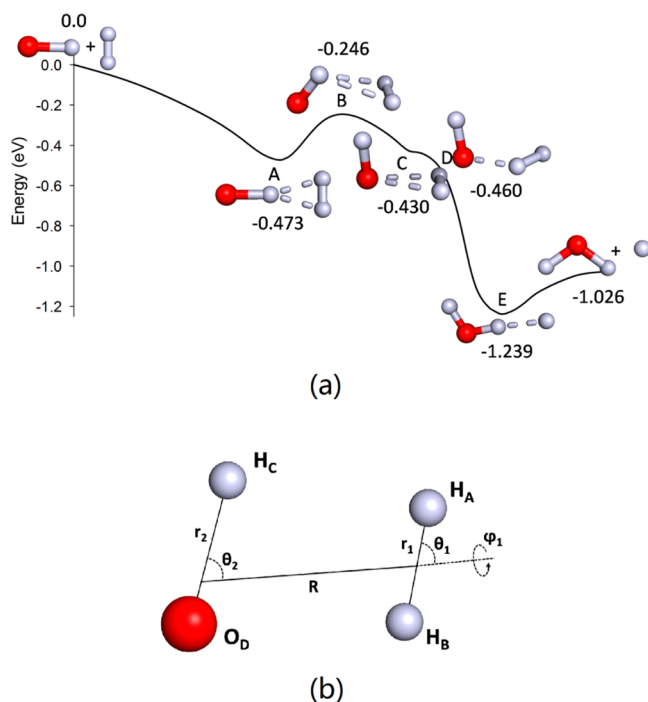


Figure 1. Reaction path of the title reaction with configurations at important points along the reaction path (a), and the full-dimensional Jacobi coordinates for the AB + CD system (b).

organized as follows. Section II outlines the theoretical methodology. The results are presented and discussed in section III. We conclude in section IV.

II. THEORY

II.A. Quantum Dynamics. The time-dependent initial state-selected wave packet (ISSWP) method employed in this study is well documented in the literature.²⁵ Here, we only briefly outline the key aspects. The full-dimensional Hamiltonian for the diatom–diatom reaction AB + CD in the reactant Jacobi coordinates, as shown in Figure 1b, for a given total angular momentum J can be written as ($\hbar = 1$ hereafter).²⁶

$$\hat{H} = -\frac{1}{2\mu_R} \frac{\partial^2}{\partial R^2} + \hat{h}_1(r_1) + \hat{h}_2(r_2) + \frac{(\hat{J} - \hat{j}_{12})^2}{2\mu_R R^2} + \frac{\hat{j}_1^2}{2\mu_1 r_1^2} + \frac{\hat{j}_2^2}{2\mu_2 r_2^2} + \hat{V}(R, r_1, r_2, \theta_1, \theta_2, \varphi_1) - V_1^{\text{ref}}(r_1) - V_2^{\text{ref}}(r_2) \quad (1)$$

where R is the distance between the centers of mass (COMs) of AB and CD, r_1 is the bond distance of AB, and r_2 is the bond distance of CD. Their corresponding reduced masses are denoted as μ_R , μ_1 , and μ_2 , respectively. \hat{j}_1 and \hat{j}_2 are the rotational angular momentum operators of AB and CD, respectively, and they are coupled to \hat{j}_{12} . \hat{J} is the total angular momentum operator of the system. $\hat{h}_i(r_i)$ are the one-dimensional (1D) reference Hamiltonians, which are defined as

$$\hat{h}_i(r_i) = -\frac{1}{2\mu_i} \frac{\partial^2}{\partial r_i^2} + V_i^{\text{ref}}(r_i) \quad i = 1, 2 \quad (2)$$

where $V_i^{\text{ref}}(r_i)$ is the corresponding 1D reference potential along the coordinate r_i .

The parity (ϵ) adapted wave function is expanded in terms of the body-fixed (BF) ro-vibrational basis functions:

$$\psi^{JMe}(\vec{R}, \vec{r}_1, \vec{r}_2) = \sum_{n, \nu_1, \nu_2, K} F_{n\nu_1\nu_2K}^{JMe} u_n^{\nu_1}(R) \phi_{\nu_1}(r_1) \phi_{\nu_2}(r_2) \times \Phi_{jK}^{JMe}(\hat{R}, \hat{r}_1, \hat{r}_2) \quad (3)$$

where n labels the translational basis functions, ν_1 and ν_2 are the basis indices for r_1 and r_2 , j denotes (j_1, j_2, J) . The translational basis function, $u_n^{\nu_1}$, is dependent on ν_1 due to the use of an L -shaped grid.²⁷ Φ_{jK}^{JMe} in eq 3 is the parity-adapted coupled BF total angular momentum eigenfunction, which can be written as

$$\Phi_{jK}^{JMe} = (1 + \delta_{K0})^{-1/2} \sqrt{\frac{2J+1}{8\pi}} [D_{K,M}^{J*} Y_{j_1 j_2}^{j_1 j_2 K} + \epsilon(-1)^{j_1+j_2+j_{12}+J} D_{-K,M}^{J*} Y_{j_1 j_2}^{j_1 j_2 -K}] \quad (4)$$

where $D_{K,M}^J$ is the Wigner rotation matrix.²⁸ M is the projection of J on the space-fixed z axis, and K is its projection on the BF z axis that coincides with R . $Y_{j_1 j_2}^{j_1 j_2 K}$ is the eigenfunction of \hat{j}_{12} defined as

$$Y_{j_1 j_2}^{j_1 j_2 K} = \sum_{\omega} \langle j_1 \omega j_2 K - \omega | j_{12} K \rangle y_{j_1 \omega}(\hat{r}_1) y_{j_2 K-\omega}(\hat{r}_2) \quad (5)$$

and y_{jm} denotes the spherical harmonics. Note the restriction that $\epsilon(-1)^{j_1+j_2+j_{12}+J} = 0$ for $K = 0$ in eq 4.

The centrifugal potential, i.e., $(\hat{J} - \hat{j}_{12})^2 / 2\mu_R R^2$ in the Hamiltonian, which gives rise to the coupling between different K blocks in the BF representation, is given by

$$\begin{aligned} \langle \Phi_{jK}^{JMe} | (\hat{J} - \hat{j}_{12})^2 | \Phi_{j'K'}^{JMe} \rangle \\ = \delta_{jj'} \{ \delta_{KK'} [J(J+1) + j_{12}(j_{12}+1) - 2K^2] \\ - \delta_{K+1K'} \lambda_{jK}^+ \lambda_{jK'}^+ (1 + \delta_{K0})^{1/2} \\ - \delta_{K-1K'} \lambda_{jK}^- \lambda_{jK'}^- (1 + \delta_{K1})^{1/2} \} \end{aligned} \quad (6)$$

and the quantity λ is defined as $\lambda_{AB}^{\pm} = [A(A+1) - B(B+1)]^{1/2}$.

Within the centrifugal sudden (CS) approximation,^{29,30} the coupling between different K blocks is neglected, thus K becomes a good quantum number and is conserved. This approximation has been widely used in quantum scattering calculations and the results for activated bimolecular reactions have been reasonably accurate, but the accuracy deteriorates for barrierless complex-forming reactions.³¹ As a result, it is important to test its validity in different reactions.

The initial wave packet is constructed by the direct product of a localized Gaussian wave packet in the scattering coordinate and a specific ($JK\epsilon$) state of the reactive system with specific ro-vibrational states of both H_2 and OH^+ and the form and parameters are given in Table 1. The wave packet is propagated in time using a second-order split-operator method.³² The flux through the dividing surface, $S[r_1=r_1^*]$, is obtained from the energy-dependent scattering wave function, $\psi_i^{\dagger}(E)$, which is determined by Fourier transforming the time-dependent wave packet at the dividing surface, placed in the product arrangement channel. In each step, the wave packet is transformed between different representations that diagonalized various terms in the Hamiltonian.³³ Finally, the wave packet is absorbed at the edges of the grid using a negative

Table 1. Numerical Parameters Used in the Wave Packet Calculations (Atomic Units Used unless Stated Otherwise)

	H ₂ + OH ⁺	HD/D ₂ + OH ⁺
grid/basis range and size	$R \in [0.8, 18.5], N_R^{\text{tot}} = 160, N_R^{\text{int}} = 50$ $N_{r_1}^{\text{int}} = 33, N_{r_1}^{\text{asy}} = 5, N_{r_2} = 3$ $j_{1\text{max}} = 40, j_{2\text{max}} = 28$	$R \in [0.8, 18.5], N_R^{\text{tot}} = 176, N_R^{\text{int}} = 55$ $N_{r_1}^{\text{int}} = 37, N_{r_1}^{\text{asy}} = 5, N_{r_2} = 3$ $j_{1\text{max}} = 44, j_{2\text{max}} = 28$
initial wave packet ^a	$R_0 = 16.0, \delta = 0.25, E_i = 0.5 \text{ eV}$	$R_0 = 16.0, \delta = 0.25, E_i = 0.35 \text{ eV}$
absorbing potential ^b	$R_a = 16.0, \alpha_R = 0.05, n_R = 1.5$ $r_{1a} = 4.0, \alpha_{r_1} = 0.05, n_{r_1} = 1.5$	$R_a = 16.0, \alpha_R = 0.05, n_R = 1.5$ $r_{1a} = 4.0, \alpha_{r_1} = 0.05, n_{r_1} = 1.5$
flux position	$r_1^{\text{F}} = 4.0$	$r_1^{\text{F}} = 4.0$

^aInitial wave packet:

$$\varphi_{k_0}(R) = \left(\frac{1}{\pi\delta^2}\right)^{1/4} e^{-(R-R_0)^2/2\delta^2} e^{-ik_0 R}$$

^bAbsorbing potential:

$$F_{\text{abs}} = e^{-\Delta t \alpha [(x-x_a)/(x_{\text{max}}-x_a)]^n}$$

imaginary absorbing potential with the form given in Table 1 to enforce outgoing boundary conditions.

The integral cross section (ICS) from a specific initial state is calculated by summing the reaction probabilities over all the partial waves labeled by J ,

$$\begin{aligned} \sigma_{v_1 v_2 j_1 j_2}(E) &= \frac{1}{(2j_1 + 1)(2j_2 + 1)} \sum_{j_{12}} \frac{\pi}{k^2} \sum_{J \geq K} (2J + 1) P_{v_1 v_2 j_1 j_2 j_{12}}^{J, \varepsilon}(E) \\ &= \frac{1}{(2j_1 + 1)(2j_2 + 1)} \sum_{j_{12} K \varepsilon} \sigma_{v_1 v_2 j_1 j_2}^{j_{12} K \varepsilon}(E) \end{aligned} \quad (7)$$

where $\sigma_{v_1 v_2 j_1 j_2}^{j_{12} K \varepsilon}$ is defined as the j_{12} , K and ε specific cross section and K is taken from 0 to $\min(j_{12}, J)$. In this study, we focus on the dynamics from the ground vibrational states, i.e., $v_1 = v_2 = 0$. Thus, we will drop the vibrational quantum numbers hereafter.

The numerical parameters employed in the QD calculations of H₂/HD/D₂ + OH⁺ on an L-shaped grid are given in Table 1. The parameters, which were well tested to give converged results, result in a very large size for the wave packet. The total number of grid points and basis functions for our calculations is approximately 1.5×10^8 in the CS calculation and 6.0×10^8 in the CC calculation, underscoring the difficulties associated with such calculations. The propagation time is around 40000 au with a time step of 10 au.

II.B. Quasi-Classical Trajectory Method. Standard QCT calculations for the title reaction were carried out on the basis of the PES described above, using VENUS.³⁴ The total reactive ICS for the reaction was computed according to the following formula:

$$\sigma_r(E_c) = \pi b_{\text{max}}^2(E_c) P_r(E_c) \quad (8)$$

where the reaction probability at the specified collision energy E_c is given by the ratio between N_r and N_t :

$$P_r(E_c) = N_r/N_t \quad (9)$$

The reactive differential cross section (DCS) is computed by

$$\frac{d\sigma_r}{d\Omega} = \frac{\sigma_r P_r(\theta)}{2\pi \sin(\theta)} \quad (10)$$

where $P_r(\theta)$ is the normalized probability for the scattering products at the scattering angle θ , which is given by

$$\theta = \cos^{-1} \left(\frac{\vec{v}_i \cdot \vec{v}_f}{|\vec{v}_i| |\vec{v}_f|} \right) \quad (11)$$

Here, \vec{v} is the relative velocity vector, and the subscripts “i” and “f” denote “initial” and “final”, respectively, $\vec{v}_i = \vec{v}_{\text{H}_2} - \vec{v}_{\text{OH}^+}$, $\vec{v}_f = \vec{v}_{\text{H}} - \vec{v}_{\text{H}_2\text{O}}$. The signs of the relative velocity vectors were chosen such that $\theta = 0^\circ$ corresponds to forward scattering and $\theta = 180^\circ$ corresponds to backward scattering.

The trajectories were initiated with a reactant separation of 10.0 Å, and terminated when products reached a separation of 7.0 Å, or when reactants are separated by 9.0 Å for nonreactive trajectories. During the propagation, the gradient of the PES was obtained numerically by a central-difference algorithm. The propagation time step was selected to be 0.02 fs, which conserves the energy better than 0.04 kcal/mol for most trajectories. Batches of 50 000 trajectories have been run at each collision energies (from 0.05 to 1.00 eV). A few trajectories that failed to converge energy to 0.04 kcal/mol or were nonreactive after 4.0 ps were discarded. The maximal impact parameter (b_{max}) was determined using small batches of trajectories with trial values.

III. RESULTS

III.A. Accuracy of the CS Approximation. The CS approximation greatly reduces the computational costs and thus is widely employed in reaction dynamics studies of bimolecular reactions. Under the CS approximation, only one K block (i.e., the initial K) is included in the QD calculation. Here, we will test the accuracy of the CS approximation for the title reaction by comparing its cross section with the coupled-channel (CC) result. In the CC calculations, the value of K is taken from 0 to $\min(J, 2)$. Tests showed that larger K_{max} values do not change the results significantly.

The CC and CS ICSs for the reaction with the ground ro-vibrational states of both reactants are presented in Figure 2. Both are monotonically decaying functions with the collision

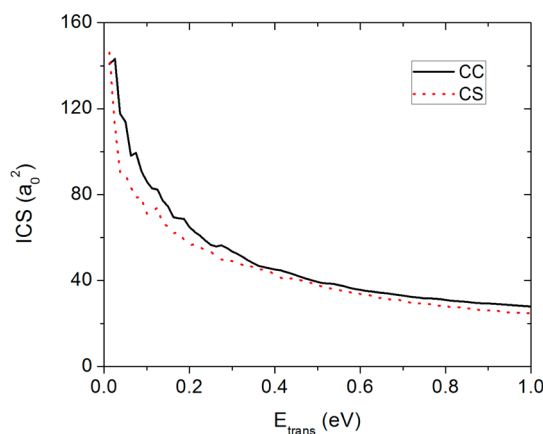


Figure 2. Comparison of the CS and CC ICSs for the H₂($j_1=0$) + OH⁺($j_2=0$) reaction as a function of the collision energy.

energy, consistent with the barrierless nature of the reaction. The small kinks at low collision energy are presumably due to resonances supported by the well in the entrance channel (Figure 1a). From the figure, it is clear that the CS cross section is slightly but noticeably smaller than the CC counterpart over the entire collision energy range. The relative error is less than 14% at collision energies larger than 0.2 eV whereas it runs up to 25% at low collision energies. The errors, which are presumably caused by the fact that the shallow well in the entrance valley (Figure 1a) strengthens the Coriolis coupling among the helicity channels, are acceptable. Given the significant savings associated with the CS approximation, we report below the results obtained with this approximation.

III.B. Rotational Effects of H_2 and OH^+ . Figure 3a shows the QD and QCT ICSs for the $H_2(j_1=0-2) + OH^+(j_2=0)$

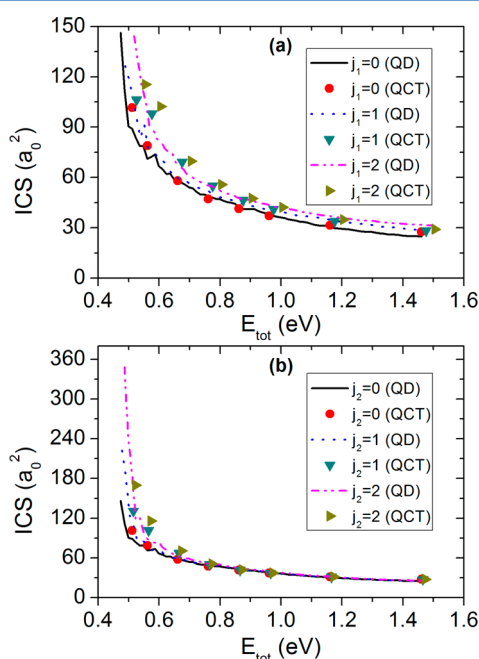


Figure 3. QD and QCT ICSs for the $H_2(j_1=0-2) + OH^+(j_2=0-2)$ reaction as a function of total energy.

reaction as a function of total energy, which is the sum of collision and internal energies of the reactants. The QD excitation functions for the three initial rotational states of H_2 are very similar; i.e., they first decrease sharply at low energies and then become more or less flat at higher energies. On the contrary, the QD cross section increases with the H_2 rotational excitation over the entire energy range studied. In other words, low-lying rotational excitations of H_2 clearly enhance the reactivity of this reaction. These features are well reproduced by the QCT results. However, it appears that the QCT cross sections are slightly larger than the QD counterparts at low energies.

The QD and QCT ICSs for the $H_2(j_1=0) + OH^+(j_2=0-2)$ reaction are plotted in Figure 3b as a function of total energy. Clearly, both the QD and QCT results indicate that the rotational excitation of OH^+ significantly promotes the reaction at low energies. At higher energies, rotational excitations of OH^+ have a negligible effect on the reaction and the cross sections from the three rotational states of OH^+ are nearly indistinguishable. This feature is also found in the $H_2 + H_2O^+$ reaction, in which the enhancement effect is also much more

pronounced at low collision energies and becomes weaker at high collision energies.^{18,20,21} This trend is reproduced by QCT results shown in the same figure. It should be noted that the enhancements of the title reaction by OH^+ rotational excitations at low energies are much larger than that by H_2 rotational excitations, particularly considering the rotational constant of OH^+ (16.79 cm^{-1}) is significantly smaller than that of H_2 (60.85 cm^{-1}).

To better understand the rotational enhancement effects observed here, in Figure 4, the quantum opacity function for j_1

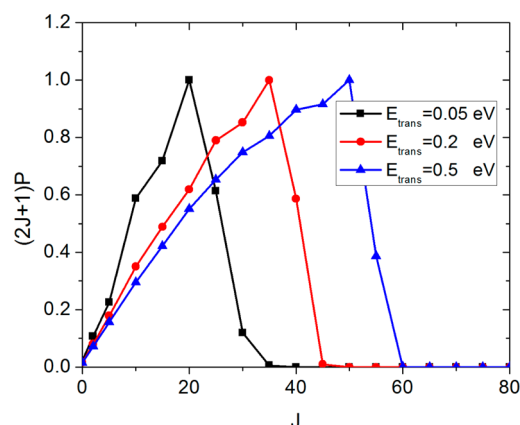


Figure 4. Quantum opacity functions for the $H_2(j_1=0) + OH^+(j_2=0)$ reaction at several selected collision energies.

$= j_2 = 0$ is plotted as a function of the total angular momentum quantum number with the translational energies at 0.05, 0.2, and 0.5 eV. The opacity functions first increase gently with the collision energy, reach maximum, and then decrease sharply. Clearly, the cross section is dominated by the partial waves near the highest J values allowed at particular energy. Now let us examine the reaction path for the title reaction at different J values. In Figure 5, the sum of the interaction potential and centrifugal potential ($J(J+1)/2\mu_R R^2$) along the minimum energy path is shown as a function of the reaction coordinate. It is clear from the figure that the effective barrier changes with the J value.

At low J values (<30), the effective barrier is close to the geometry of the submerged saddle point. As a result, this saddle

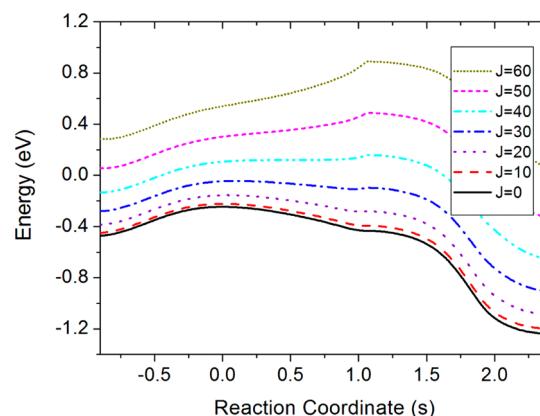


Figure 5. Sum of the interaction potential energy and the centrifugal potential energy at different total angular momentum J as a function of the reaction coordinate s . The energies are relative to the $H_2 + OH^+$ asymptote.

point serves as a bottleneck that controls low-energy collisions. This explains the rotational enhancement of the OH^+ reactant. As pointed out earlier, the OH^+ rotational mode is strongly coupled with the reaction coordinate at this saddle point, as evidenced by the large SVP projection value of 0.89.¹⁷ In other words, the reaction coordinate at the saddle point contains a large component of OH^+ rotation. Hence, exciting the OH^+ rotation effectively channels energy into the reaction coordinate, according to the SVP model,^{23,24} leading to strong enhancement of reactivity.

For higher J values, it is clear that the effective barrier moves to larger reaction coordinate values. As a result, the submerged saddle point no longer controls the reaction. This is consistent with the diminishing ability of the OH^+ rotation in enhancing the reactivity at high energies, shown in Figure 3b. In Figure 5, the effective barrier for high J values is located in a region in which the H_2 moiety undergoes some rotational motion, Figure 1a. As a result, excitation of H_2 rotation is expected to help overcome this late effective barrier, even though it does not correspond to a stationary point in the reaction path. This effect is present in all J values except very low ones, thus affects reactivity. This is presumably the underlying reason for the rotational enhancement of reactivity by H_2 .

III.C. Isotopic Substitution Effects. Figure 6 displays the QD and QCT ICSs for the $\text{H}_2/\text{HD}/\text{D}_2(j_1=0) + \text{OH}^+(j_2=0)$

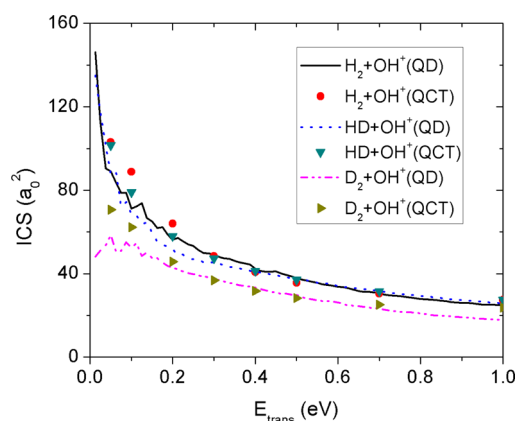


Figure 6. QD and QCT ICSs for the $\text{H}_2/\text{HD}/\text{D}_2(j_1=0) + \text{OH}^+(j_2=0)$ reaction as a function of collision energy.

reactions as a function of translational energy. From the QD results, it can be seen that the cross section of the $\text{D}_2 + \text{OH}^+$ reaction is much smaller than those of the $\text{H}_2 + \text{OH}^+$ and $\text{HD} + \text{OH}^+$ reactions. The cross section of the $\text{HD} + \text{OH}^+$ reaction is comparable to that of the $\text{H}_2 + \text{OH}^+$ reaction, whereas it is visibly smaller at the middle energy ranging from 0.1 to 0.4 eV. In addition, the cross sections of both the $\text{H}_2 + \text{OH}^+$ and $\text{HD} + \text{OH}^+$ reactions drop off sharply at low collision energies and then decreases very slowly at high collision energies. In contrast, the cross section of the $\text{D}_2 + \text{OH}^+$ reaction oscillates strongly at very low collision energies and then decays smoothly as the collision energy further increases. Apparently, there exists significant isotopic substitution effect in this system, presumably due to the much larger mass of the deuterium atom and smaller zero point energy of D_2 .

The corresponding QCT ICSs are also presented in Figure 6 for comparison. For the three isotope-substituted reactions, the QCT ICSs reproduce the QD results quite well at collision energies higher than 0.3 eV, but they deviate somewhat from

the QD results at low collision energies. This can be explained by the fact that the quantum effect is pronounced, even dominant, at low energies. In addition, there exist intrinsic defects in the QCT methodology, i.e., the leakage of zero-point energy (ZPE) and fast energy flow among various modes. The smaller QD cross sections than the QCT counterparts at low collision energies presumably result from the CS approximation employed in the QD calculation. As shown in Figure 2, the exact CC cross section is visibly larger than the CS cross section within the low collision energy range. Overall, the quantum-classical agreement is quite good, and the QCT calculations capture the main features of the QD results, including the much lower ICS for the $\text{D}_2 + \text{OH}^+$ reaction and the similar ICSs for the $\text{H}_2 + \text{OH}^+$ and $\text{HD} + \text{OH}^+$ reactions.

III.D. Differential Cross Section. The differential cross section (DCS) for the $\text{H}_2(j_1=0) + \text{OH}^+(j_2=0)$ reaction calculated using the QCT method is shown in Figure 7 with

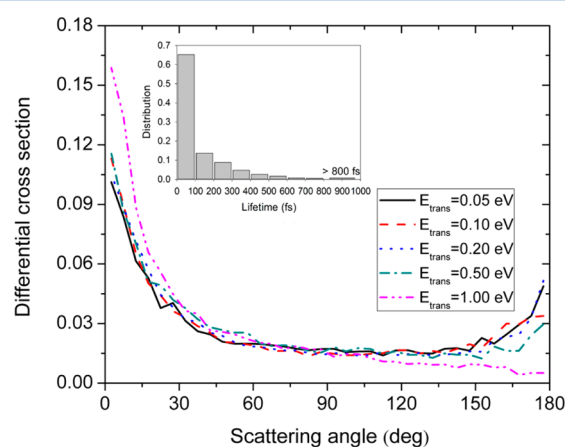


Figure 7. QCT DCSs for the $\text{H}_2(j_1=0) + \text{OH}^+(j_2=0)$ reaction at the collision energy of 0.05, 0.10, 0.20, 0.50, and 1.00 eV. Distributions are normalized. The inset shows the lifetime distribution of trajectories at 0.10 eV of collision energy.

the collision energy at 0.10, 0.20, 0.50 and 1.00 eV. Clearly, the scattering is mostly dominated by both the forward and backward directions, but with a forward bias. This is consistent with the complex-forming mechanism of this reaction. The asymmetry of the DCS suggests that the lifetime of the H_3O^+ complex is quite short, which is consistent with the fast reaction time of the trajectories. Indeed, in the same figure, the lifetime distribution of the reaction with a collision energy of 0.10 eV is shown and the reaction is apparently very fast. The lifetime is defined as the time spent by a trajectory starting as the distances between O atom and H_A or H_B are both less than 3.0 Å (the entrance of the pre-reaction well) and ending when the $\text{H}_\text{A}-\text{H}_\text{B}$ distance becomes larger than 2.0 Å (the exit of the product channel). Indeed, the backward peak disappears at high collision energies, suggesting the gradual transition to a direct abstraction mechanism. As discussed above, the reaction is dominated by large J values and thus large impact parameters. For such collisions, the stripping mechanism dominates, resulting in forward scattering.

IV. CONCLUSIONS

In this work, both QD and QCT calculations of $\text{H}_2 + \text{OH}^+ \rightarrow \text{H} + \text{H}_2\text{O}^+$ reaction have been carried out on a newly developed ab initio based potential energy surface. This barrierless

reaction is found to possess many characteristics of a complex forming reaction, but the lifetime of the intermediate is quite short. Particular attention has been paid to study the reactant rotational effects and isotopic substitution effects. Most of the results reported here have been obtained using the CS approximation, which was first tested by comparing its cross section with the CC result. It was found that the CS cross section resembles well the CC profile, although it underestimates the CC result over the entire energy range studied.

By exciting the two reactants to different low-lying rotational states, we found that the rotational excitation of H_2 enhances the reaction over the entire energy range. On the contrary, the rotational excitation of OH^+ promotes the reaction markedly at low collision energies whereas it has a negligible effect at high collision energies. These rotational enhancement effects have been attributed to difference sources. The former is due to the shift of the effective barrier at large J values to a region in which the H_2 rotation is required. As a result, its excitation helps to overcome the barrier. On the contrary, the latter is attributed to the strong coupling of the OH^+ rotation to the reaction coordinate at the submerged saddle point, which controls the reaction at low J values and thus low collision energies.

Isotopic substitution effects have also been investigated by substituting the collider H_2 by HD and D_2 . Both the QM and QCT results indicated that the cross section of $\text{D}_2 + \text{OH}^+$ is lower than those of $\text{H}_2 + \text{OH}^+$ and $\text{HD} + \text{OH}^+$ whereas the cross section of $\text{H}_2 + \text{OH}^+$ is quite close to that of $\text{HD} + \text{OH}^+$ at very low and high collision energies with the former slightly larger at middle collision energies.

AUTHOR INFORMATION

Corresponding Author

*H. Guo. E-mail: hguo@unm.edu.

Present Addresses

[†]State Key Laboratory of Magnetic Resonance and Atomic and Molecular Physics, National Centre for Magnetic Resonance in Wuhan, Wuhan Institute of Physics and Mathematics, Chinese Academy of Sciences, Wuhan 430071, China.

[‡]College of Chemistry and Materials Science, Northwest University, Xi'an 710069, China.

Notes

The authors declare no competing financial interest.

ACKNOWLEDGMENTS

The authors acknowledge financial support for the Air Force Office of Scientific Research (AFOSR-FA9550-15-1-0305 to H.G.). Partial support from the National Natural Science Foundation of China (Grant No. 21203259 to A.L.) is also acknowledged. The calculations have been carried out at the Center for Advanced Research Computing (CARC) at University of New Mexico and at the National Energy Research Scientific Computer (NERSC) Center. H.G. thanks Al Viggiano for many fruitful discussions.

REFERENCES

- (1) Smith, D. The ion chemistry of interstellar clouds. *Chem. Rev.* **1992**, *92*, 1473–1485.
- (2) Fridman, A. *Plasma Chemistry*; Cambridge University Press: Cambridge, U.K., 2012.
- (3) Shuman, N. S.; Hunton, D. E.; Viggiano, A. A. Ambient and modified atmospheric ion chemistry: From top to bottom. *Chem. Rev.* **2015**, *115*, 4542–4570.
- (4) Ng, C.-Y. State-to-state spectroscopy and dynamics of ions and neutrals by photoionization and photoelectron methods. *Annu. Rev. Phys. Chem.* **2014**, *65*, 197–224.
- (5) Wester, R. Velocity map imaging of ion–molecule reactions. *Phys. Chem. Chem. Phys.* **2014**, *16*, 396–405.
- (6) Xie, J.; Otto, R.; Mikosch, J.; Zhang, J.; Wester, R.; Hase, W. L. Identification of atomic-level mechanisms for gas-phase $\text{X}^- + \text{CH}_3\text{Y}$ $\text{S}_{\text{N}}2$ reactions by combined experiments and simulations. *Acc. Chem. Res.* **2014**, *47*, 2960–2969.
- (7) Szabó, I.; Czako, G. Revealing a double-inversion mechanism for the $\text{F}^- + \text{CH}_3\text{Cl}$ $\text{S}_{\text{N}}2$ reaction. *Nat. Commun.* **2015**, *6*, 5972.
- (8) Herbst, E.; Klemperer, W. Formation and depletion of molecules in dense interstellar clouds. *Astrophys. J.* **1973**, *185*, 505–533.
- (9) Watson, W. D. Interstellar chemistry. *Acc. Chem. Res.* **1977**, *10*, 221–226.
- (10) Hollenbach, D.; Kaufman, M. J.; Neufeld, D.; Wolfire, M.; Goicoechea, J. R. The chemistry of interstellar OH^+ , H_2O^+ , and H_3O^+ : Inferring the cosmic-ray ionization rates from observations of molecular ions. *Astrophys. J.* **2012**, *754*, 105.
- (11) Neufeld, D. A.; Goicoechea, J. R.; Sonnentrucker, P.; Black, J. H.; Pearson, J.; Yu, S.; Phillips, T. G.; Lis, D. C.; De Luca, M.; Herbst, E.; et al. Herschel/HIFI observations of interstellar OH^+ and H_2O^+ towards W49N: a probe of diffuse clouds with a small molecular fraction. *Astron. Astrophys.* **2010**, *521*, L10.
- (12) Gerin, M.; De Luca, M.; Black, J.; Goicoechea, J. R.; Herbst, E.; Neufeld, D. A.; Falgarone, E.; Godard, B.; Pearson, J. C.; Lis, D. C.; et al. Interstellar OH^+ , H_2O^+ and H_3O^+ along the sight-line to G10.6–0.4. *Astron. Astrophys.* **2010**, *518*, L110.
- (13) Gonzalez-Alfonso, E.; Fischer, J.; Bruderer, S.; Muller, H. S. P.; Gracia-Carpio, J.; Sturm, E.; Lutz, D.; Poglitsch, A.; Feuchtgruber, H.; Veilleux, S.; et al. Excited OH^+ , H_2O^+ , and H_3O^+ in NGC 4418 and Arp 220. *Astron. Astrophys.* **2013**, *550*, A25.
- (14) Martinez, O.; Ard, S. G.; Li, A.; Shuman, N. S.; Guo, H.; Viggiano, A. A. Temperature-dependent kinetic measurements and quasi-classical trajectory studies for the $\text{OH}^+ + \text{H}_2/\text{D}_2 \rightarrow \text{H}_2\text{O} + \text{HDO}^+ + \text{H/D}$ reactions. *J. Chem. Phys.* **2015**, *143*, 114310.
- (15) Jiang, B.; Guo, H. Permutation invariant polynomial neural network approach to fitting potential energy surfaces. *J. Chem. Phys.* **2013**, *139*, 054112.
- (16) Li, J.; Jiang, B.; Guo, H. Permutation invariant polynomial neural network approach to fitting potential energy surfaces. II. Four-atom systems. *J. Chem. Phys.* **2013**, *139*, 204103.
- (17) Li, A.; Guo, H. A full-dimensional ab initio global potential energy surface of $\text{H}_3\text{O}^+(\tilde{a}^3\text{A})$ for the $\text{OH}^+(\tilde{X}^3\Sigma^-) + \text{H}_2(\tilde{X}^1\Sigma_g^+) \rightarrow \text{H}(\tilde{2}\text{S}) + \text{H}_2\text{O}^+(\tilde{X}^2\text{B}_1)$ reaction. *J. Phys. Chem. A* **2014**, *118*, 11168–11176.
- (18) Li, A.; Li, Y.; Guo, H.; Lau, K.-C.; Xu, Y.; Xiong, B.; Chang, Y.-C.; Ng, C. Y. Communication: The origin of rotational enhancement effect for the reaction of $\text{H}_2\text{O}^+ + \text{H}_2 (\text{D}_2)$. *J. Chem. Phys.* **2014**, *140*, 011102.
- (19) Li, A.; Guo, H. A nine-dimensional ab initio global potential energy surface for the $\text{H}_2\text{O}^+ + \text{H}_2 \rightarrow \text{H}_3\text{O}^+ + \text{H}$ reaction. *J. Chem. Phys.* **2014**, *140*, 224313.
- (20) Xu, Y.; Xiong, B.; Chang, Y. C.; Ng, C. Y. Communication: Rovibrationally selected absolute total cross sections for the reaction $\text{H}_2\text{O}^+(\text{X}^2\text{B}_1; v_1^+v_2^+v_3^+ = 000; \text{N}^+\text{K}_a^+\text{K}_c^+) + \text{D}_2$: Observation of the rotational enhancement effect. *J. Chem. Phys.* **2012**, *137*, 241101.
- (21) Xu, Y.; Xiong, B.; Chang, Y. C.; Ng, C. Y. The translational, rotational, and vibrational energy effects on the chemical reactivity of water cation $\text{H}_2\text{O}^+(\text{X}^2\text{B}_1)$ in the collision with deuterium molecule D_2 . *J. Chem. Phys.* **2013**, *139*, 024203.
- (22) Ard, S. G.; Li, A.; Martinez, O.; Shuman, N. S.; Viggiano, A. A.; Guo, H. Experimental and theoretical kinetics for the $\text{H}_2\text{O}^+ + \text{H}_2/\text{D}_2 \rightarrow \text{H}_3\text{O}^+/\text{H}_2\text{DO}^+ + \text{H/D}$ reactions: Observation of the rotational Effect in the temperature dependence. *J. Phys. Chem. A* **2014**, *118*, 11485–11489.
- (23) Jiang, B.; Guo, H. Relative efficacy of vibrational vs. translational excitation in promoting atom-diatom reactivity: Rigorous examination

of Polanyi's rules and proposition of sudden vector projection (SVP) model. *J. Chem. Phys.* **2013**, *138*, 234104.

(24) Guo, H.; Jiang, B. The sudden vector projection model for reactivity: Mode specificity and bond selectivity made simple. *Acc. Chem. Res.* **2014**, *47*, 3679–3685.

(25) Zhang, J. Z. H. *Theory and Application of Quantum Molecular Dynamics*; World Scientific: Singapore, 1999.

(26) Zhang, D. H.; Zhang, J. Z. H. Full-dimensional time-dependent treatment for diatom-diatom reactions: The $\text{H}_2 + \text{OH}$ reaction. *J. Chem. Phys.* **1994**, *101*, 1146–1156.

(27) Zhang, D. H.; Zhang, J. Z. H. Accurate quantum calculations for the benchmark reaction $\text{H}_2 + \text{OH} \rightarrow \text{H}_2\text{O} + \text{H}$ in five-dimensional space: reaction probability for $J = 0$. *J. Chem. Phys.* **1993**, *99*, 5615–5618.

(28) Zare, R. N. *Angular Momentum*; Wiley: New York, 1988.

(29) Pack, R. T. Space-fixed vs body-fixed axes in atom-diatomic molecule scattering. Sudden approximations. *J. Chem. Phys.* **1974**, *60*, 633–639.

(30) McGuire, P.; Kouri, D. J. Quantum mechanical close coupling approach to molecular collisions. j_z -conserving coupled states approximation. *J. Chem. Phys.* **1974**, *60*, 2488–2499.

(31) Guo, H. Quantum dynamics of complex-forming bimolecular reactions. *Int. Rev. Phys. Chem.* **2012**, *31*, 1–68.

(32) Feit, M. D.; Fleck, J. A. Solution of the Schrodinger equation by a spectral method II: Vibrational energy levels of triatomic molecules. *J. Chem. Phys.* **1983**, *78*, 301.

(33) Light, J. C.; Carrington, T., Jr. Discrete-variable representations and their utilization. *Adv. Chem. Phys.* **2000**, *114*, 263–310.

(34) Hu, X.; Hase, W. L.; Pirraglia, T. Vectorization of the general Monte Carlo classical trajectory program VENUS. *J. Comput. Chem.* **1991**, *12*, 1014–1024.